

KRATTA, A TRIPLE TELESCOPE ARRAY FOR THE ASY-EOS EXPERIMENT

J. Łukasik^{a,*}, P. Pawłowski^a, A. Budzanowski^{a,†}, B. Czech^a, I. Skwirczyńska^a,
J. Brzychczyk^b, M. Adameczyk^b, S. Kupny^b, P. Lasko^b, Z. Sosin^b, A. Wieloch^b, M. Kiš^c,
Y. Leifels^c, W. Trautmann^c and the ASY-EOS Collaboration

a) Institute of Nuclear Physics, IFJ-PAN, 31-342 Kraków, Poland

b) Institute of Physics, Jagiellonian University, 30-059 Kraków, Poland

c) GSI, D-64291 Darmstadt, Germany

Abstract

A new detection system KRATTA, Kraków Triple Telescope Array, is presented. This versatile, low threshold, broad energy range system has been built to measure the energy, emission angle, and isotopic composition of light charged reaction products. It has been equipped with fully digital chains of electronics. The array performed very well during the ASY-EOS experiment, conducted in May 2011 at GSI. The performance of the array is presented using the first experimental results, with the emphasis on the advantages of the pulse shape analysis.

1. Motivation and requirements

The main parameters of the KRATTA array have been motivated by the needs of the ASY-EOS experiment [1]. This experiment has been designed to study the density dependence of the nuclear symmetry energy by measuring flows and isotopic compositions of the reaction products from the $^{197}\text{Au}+^{197}\text{Au}$, $^{96}\text{Ru}+^{96}\text{Ru}$, and $^{96}\text{Zr}+^{96}\text{Zr}$ reactions at 400 MeV/nucleon. During the experiment the most relevant products, neutrons and $Z=1$ and 2 particles, have been measured by the LAND [2] detector and the direction and magnitude of the impact vector were estimated using the CHIMERA [3] and ALADIN ToF-Wall [4] detectors. The KRATTA array has been designed to complement the neutron and hydrogen detection with LAND by measuring the isotopic composition and flow of light charged reaction products up to atomic number $Z \lesssim 7$, and specially, to identify the hydrogen and helium isotopes with a resolution much better than achievable with LAND. The array was placed on the opposite side of the beam with respect to LAND, and covered approximately the same solid angle (160 msr). It has been designed to detect energetic particles emerging from the “mid-rapidity” region of the 400 MeV/nucleon reactions. Modular design, portability, low thresholds (below 3 MeV/nucleon) and high maximum energy (~ 260 MeV/nucleon for p and α), allow the array to be used in various configurations and experiments. In particular, it will very well suit the needs of the future cyclotron facility at IFJ-PAN in Kraków, planned for proton beams from 70 to 250 MeV.

2. Active elements and geometry

The modules of KRATTA are composed of three large area HAMAMATSU PIN photodiodes for direct detection [5] and of two CsI(Tl) crystals [6]. The layout and dimensions of these active elements are presented in Fig. 1 and their main characteristics are summarized in Table 1.

The first photodiode (PD0 in Fig. 1) serves as a Si ΔE detector providing the ionization

*E-mail: jerzy.lukasik@ifj.edu.pl

†Deceased.

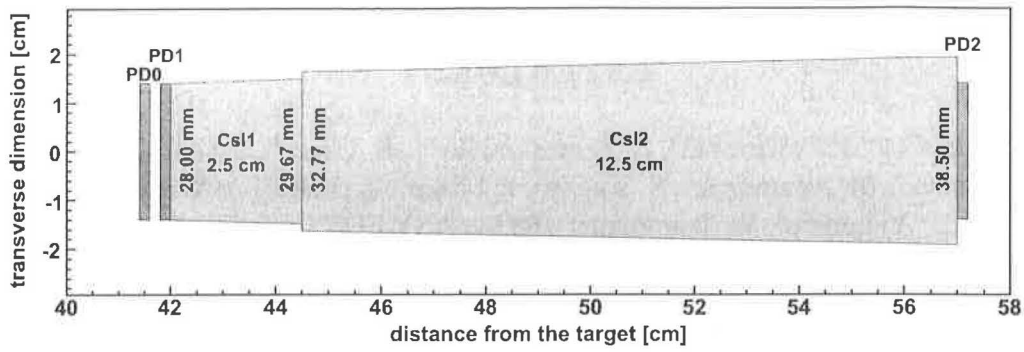


Figure 1: Schematic layout of the active elements.

Photodiodes [5]		CsI(Tl) Crystals [6]	
Active Area	28×28 mm ²	Tl concentration	1500 ppm
Thickness	500±15 μm	LO non-uniformity	< 7 %
Dead Layers	1.5 μm front 20 μm rear	Shape	Truncated pyramids
Full Depletion	120-135 V	Tolerance	±0.1 mm
Dark Current	6-16 nA	Wrapping [8]	
Rise Time	40 ns	Reflectance	> 98 %
Capacitance	190±3 pF	Thickness	65 μm

Table 1: Main characteristics of the active elements

signal alone. It has been “reverse mount”, i.e. the ohmic side towards the incoming particles. The second photodiode (PD1), naturally “reverse mount”, works in a “Single Chip Telescope”, SCT [7], configuration and provides a composite signal combined of a direct (ionization) component and of a scintillation component coming from the thin crystal (CsI1). The third photodiode (PD2) reads out the light from the thick crystal (CsI2) and, in addition, provides an ionization signal for particles that punch through the crystal within its active area.

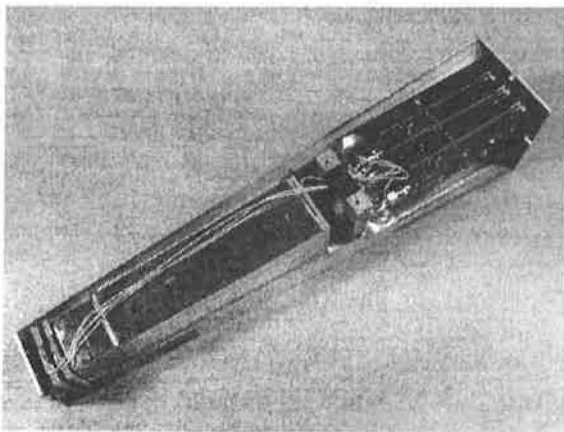


Figure 2: Single module content.

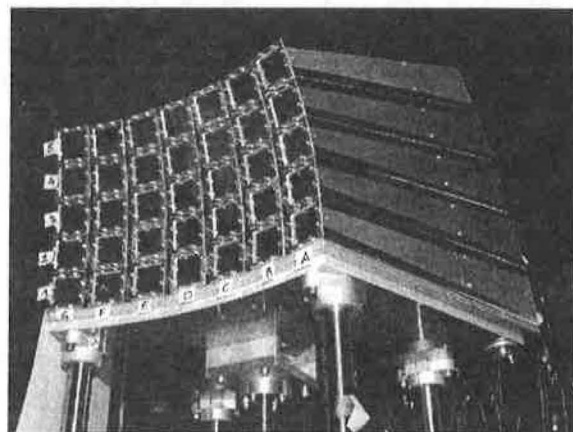


Figure 3: KRATTA in a 7×5 configuration.

The crystals have been polished and wrapped with a highly reflective ESR [8] foil, except

Fragment	E_{low}	E_{int}	E_{up}
^1H	8.3	89.6	254.4
^4He	8.3	89.4	253.9
^7Li	9.5	103.6	296.5
^{20}Ne	19.9	231.3	719.0
^{43}Ca	26.7	339.7	1134.2
^{91}Zr	34.0	513.9	1911.8
^{197}Au	38.6	775.8	3550.9

Table 2: Lower, E_{low} and intermediate, E_{int} , thresholds and upper limits, E_{up} , for selected species (in MeV/u). The thresholds correspond to the energy losses in 500 μm of Si, in 1000 μm of Si + 2.5 cm of CsI and in 1000 μm of Si + 15 cm of CsI, respectively. They have been calculated using the ATIMA tables [9].

for the front and back windows. The windows have been protected with 6 μm Mylar foils. The crystals were optically decoupled. The photodiode chips have been glued onto custom-made PCB frames and put in close optical contact with the crystal windows. The active elements have been placed inside aluminum boxes together with the charge preamplifiers (see Fig. 2). The photodiode frames and the aluminum housing reduced the geometric acceptance of a single module to about 54%. The active solid angle of a module amounts to 4.5 msr. The entrance window has been made of a 100 μm thick copper foil. During the experiment, 35 modules have been arranged in a 7 \times 5 array (Fig. 3), all placed at a radial distance of 40 cm from the target, and operated in air. In a spherical coordinate system, with the origin at the target and the beam axis defining the reference equatorial plane, the columns follow the meridians from the beam level up to about 27 $^\circ$ elevation (latitude) and the rows span the azimuth angles (longitude) between 21 $^\circ$ and 64 $^\circ$ with respect to the beam direction. The energy thresholds resulting from the thicknesses of the consecutive active layers are summarized in Table 2. As will be shown later on, the low threshold can be further reduced by applying a pulse shape analysis to the ionization signals of PD0.

3. Electronics and data acquisition

The main electronics and data acquisition functions are presented schematically in Fig. 4. The photodiodes (3 per module) have been reverse biased at 120 V, using the in-house made 120-channel, remote controlled, high voltage power supplies. The signal from each photodiode has been integrated with the own-design, low noise, charge preamplifier [10].

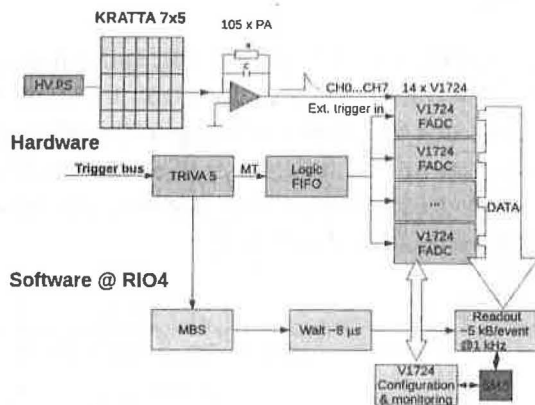


Figure 4: Analog, logical and digital signal flow chart. HV PS - high voltage power supply. PA - charge sensitive preamplifier. V1724 - CAEN digitizers. TRIVA5 - VME Trigger Synchronization Module [12]. MT - master trigger. FIFO - logical Fan-In Fan-Out module. RIO4 - VME controller board [13] running LynxOS. MBS - Multi Branch System, a GSI acquisition standard [14]. SMS - Shared Memory Segment.

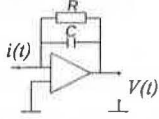
The preamps were supplied with ± 6 V and their dynamic range spanned about 3.6 V. Three nominal charge gains of the preamplifiers have been used, depending on the azimuthal angle of the module: 44.5, 22.2 and 13.5 mV/MeV, with 1, 2 and 3.3 pF feedback capacitors,

respectively. After optional amplification, the signals have been digitized with the 100 MHz, 14 bit digitizers [11] and stored for the off line analysis. All logical and digital electronics modules shown in Fig. 4 have been controlled with the RIO4 board [13] within a single VME crate. During the experiment, the 14 Flash ADC boards have been triggered with an external trigger split and delivered into each FADC module. The stored waveforms spanned 5.12 or 10.24 μs (512 or 1024 time bins), with a 2 μs pre-trigger enabling a precise baseline estimation. The shorter samples have been sufficient for the first photodiode supplying the fast ionization signal alone. The expected data throughput amounted to about 5 MB/s, assuming 1 kHz single hit rate. The actual data rate did not go beyond this estimate during the experiment. The digitizers have been remotely set up and monitored using a self-developed software. The data flow has been controlled using the standard GSI MBS system [14].

4. Pulse shape analysis

The pulse shape analysis has two main purposes in the case of KRATTA data. First of all, it has to enable the decomposition of the signals from the middle photodiode, PD1 (SCT), into the ionization and scintillation components. Secondly, it is used to resolve masses of particles stopped in the first photodiode, PD0, utilizing the relation between the range of a particle and the time characteristics of the induced current signal [15].

The following assumptions have been made to accomplish these two goals. The preamplifier response has been modeled using a simple parallel RC circuit approximation [16]:



$$\frac{i(t)}{C} = \frac{dV(t)}{dt} + \frac{V(t)}{RC} \quad (1)$$

where, RC is the feedback coupling time constant, $i(t)$ is the induced current due to the carrier motion in the photodiode, and $V(t)$ is the measured voltage pulse. This relation assumes an infinite open loop gain, small detector capacitance and a zero rise time of the charge integrator, which is an idealization, but enables an analytical approach. The induced current has been approximated with one direct (ionization), $i_D(t)$, and two scintillation, $i_{Sk}(t)$, components, all of the same form:

$$i_D(t) = Q_D \frac{e^{-t/\tau_{RD}} - e^{-t/\tau_{FD}}}{\tau_{RD} - \tau_{FD}}, \quad (2)$$

$$i_{Sk}(t) = Q_{Sk} \frac{e^{-t/\tau_{RS}} - e^{-t/\tau_{Fk}}}{\tau_{RS} - \tau_{Fk}}, \quad k = 1, 2 \quad (3)$$

where Q 's are the induced charges and the τ_{RD} , τ_{RS} and the τ_{FD} , τ_{Fk} are the rise and fall times for the respective component. The assumed shapes attempt to account for both, the complicated actual current pulse shape induced by the electrons and holes drifting in the photodiode [15], and for the instrumental rise time of the preamp. With the assumed preamplifier response (1) and the current shapes (2) and (3), it was possible to obtain the corresponding analytical model shapes of the waveforms, $V(t) = V_0 + V_D(t) + V_S(t)$, with:

$$V_D(t) = RC Q_D \left(\frac{e^{-\Delta t/RC} RC}{(RC - \tau_{RD})(RC - \tau_{FD})} + \frac{e^{-\Delta t/\tau_{RD}} \tau_{RD}}{(\tau_{RD} - RC)(\tau_{RD} - \tau_{FD})} + \frac{e^{-\Delta t/\tau_{FD}} \tau_{FD}}{(\tau_{FD} - \tau_{RD})(\tau_{FD} - RC)} \right) \quad (4)$$

$$V_S(t) = RC \sum_{k=1}^2 Q_{Sk} \left(\frac{e^{-\Delta t/RC} RC}{(RC - \tau_{RS})(RC - \tau_{Fk})} + \frac{e^{-\Delta t/\tau_{RS}} \tau_{RS}}{(\tau_{RS} - RC)(\tau_{RS} - \tau_{Fk})} + \frac{e^{-\Delta t/\tau_{Fk}} \tau_{Fk}}{(\tau_{Fk} - \tau_{RS})(\tau_{Fk} - RC)} \right) \quad (5)$$

where, for generalization, V_0 is the baseline and $\Delta t = t - t_0$, with t_0 being the beginning of the pulse.

The two scintillation components (5) have been introduced to account for the fast and slow decay modes of the CsI(Tl) crystals. The rise times, τ_{RD} and τ_{RS} , account for the photodiode, scintillator and the preamp rise times. Overall, the model depends on 11 parameters listed in Table 3.

	Parameter		Value
Q_D	Amplitude		fitted
τ_{RD}	Rise time	~ 90 ns	fixed/fitted
τ_{FD}	Fall time	< 300 ns	fixed/fitted
Q_{S1}	Fast component amplitude		fitted
Q_{S2}	Slow component amplitude		fitted
τ_{F1}	Fast fall time	~ 650 ns	fitted
τ_{F2}	Slow fall time	~ 3.2 μ s	fixed
τ_{RS}	Rise time	~ 140 ns	fixed
RC	Preamp fall time constant	~ 6 μ s	fixed
t_0	Time offset	~ 2 μ s	fitted
V_0	Baseline		fitted

Table 3: 11 parameters of the model waveforms.

The preamp fall time constant parameter RC has been determined individually for each chip by selecting the pulses with the fast ionization component alone. In order to describe precisely the shapes due to particles stopped in the first photodiode, PD0, both the time constants, τ_{RD} and τ_{FD} , were fitted and the scintillation components were obviously not used. In case of PD1 and PD2, the rise and fall times τ_{RD} and τ_{FD} were fixed. The fits were done using the FUMILI [17] minimization package, a relatively fast and precise implementation of the Gauss-Newton algorithm. Constraining some of the parameters was found inevitable, not only to obtain a good description of the waveforms (χ^2) but, at the same time, to maintain the global agreement between the reconstructed amplitudes of the three components and the predictions of the range-energy tables (see discussion of Figs. 16, 17).

An additional advantage of using the digitization of the signals and the fitting method, was the knowledge of the actual charges Q for each component, irrespectively of the substantial *ballistic deficit* (reduction of the amplitude) due to a relatively short discharge time of the preamps ($RC \simeq 6$ μ s). For instance, the sum $Q_{S1} + Q_{S2}$ represents the total light produced in the scintillators. For typical values of the parameters presented in Table 3, the ballistic deficit amounts to about 5-15% for the ionization signal and to about 25 and 50% for the fast and slow CsI(Tl) components, respectively. Usually, the fall time constant of the preamp is a compromise between the level of pile-ups, the baseline variation, and the ballistic deficit. However, since ballistic deficit is not an issue in our approach, the short preamp fall times, of the order of the time span of the waveform and of the slow CsI(Tl) decay time, have the additional advantage of making the maximum and the tail of the pulse visible within the digitized sample.

Waveforms of low energy particles stopped in the first photodiode, PD0, have been fitted with a single component of the form (4), with the time constant parameters treated as free fit parameters. A more precise time characteristics of the associated current pulse (2) was needed to perform a pulse shape based identification (see discussion of Fig. 13).

The quality of the fits is demonstrated in Fig. 5. The ordinate represents the measured voltage, in the FADC channels. The hits corresponding to the selected waveforms are also marked in the identification maps presented in the next section.

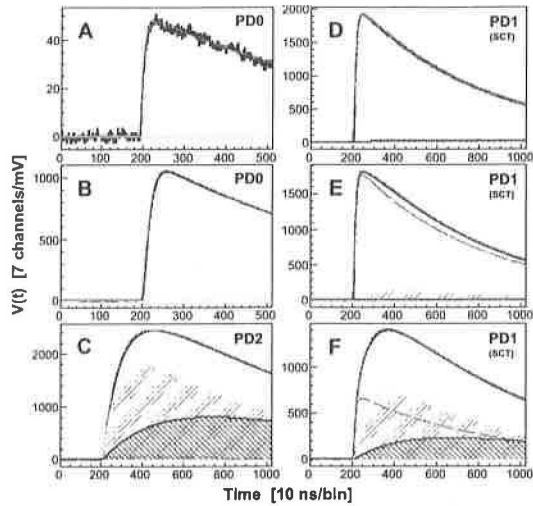


Figure 5: Example waveforms and their decomposition. Histogram (when visible): measured waveform. Solid line: sum of all fit components. Dashed line: ionization component. Hatched areas: fast and slow CsI(Tl) scintillation components. A: low-energy electron, particle or gamma ray, barely above the acquisition threshold, stopped in PD0 (see corresponding hit in Fig. 13). B: α particle stopped in PD0 (see Fig. 13). C: α particle stopped in CsI2 (see Fig. 7, 12). D: α particle stopped in PD1 (see Figs. 6, 8, 9,11). E: α particle barely punching through PD1 and stopped in CsI1 (see Figs. 6, 8, 10, 11). F: higher energy α particle stopped in CsI1 (see Figs. 6, 8, 10, 11.)

Panel A of Fig. 5 shows a waveform for a low energy electron, particle or gamma, registered barely above the acquisition threshold and stopped in PD0 (see also Fig. 13). Here the measured histogram is visible and the deviations from the smooth fit visualize the level of the total noise. The resultant signal distortions, including the photodiode, preamplifier, FADC and pickup noise sources, have been observed on the level of 0.4 mV rms, corresponding to about 30 keV.

Panel B of Fig. 5 presents the quality of the fit with the shape given by an ionization component alone (4), applied to particles stopped in PD0. Its location in the identification map is presented in Fig. 13. This fit allowed for derivation of both, the rise and fall times and, therefore, also of the *mode* (position of maximum) of the associated current signal (2):

$$mode = \frac{\tau_{RD} \tau_{FD}}{\tau_{RD} - \tau_{FD}} \log \frac{\tau_{RD}}{\tau_{FD}} \quad (6)$$

Panel C of Fig. 5 shows the waveform of a high energy α particle stopped in the CSI2 crystal. The corresponding hit has been marked in Figs. 7 and 12.

Panels D-E-F of Fig. 5 show the evolution of the pulse shape of an α particle detected and stopped in the SCT as its energy increases. The corresponding hits have been marked, when possible, in Figs. 6, 8-11.

5. Performance

Figures 6-13 present various identification (ID) maps obtained by using the parameters of the reconstructed waveform components. The strongest lines in Figs. 6-13 correspond to p , d , t , ${}^3\text{He}$, α , and so on, from bottom to top, respectively (see Fig. 16 for precise labeling).

The reconstructed amplitude maps for the first two and the last two photodiodes of the KRATTA module are presented in Figs. 6 and 7.

The identification map in Fig. 6 shows a complex spectrum with each “ID-line” composed of two parts: an ordinary Si-Si hyperbolic segment at low energies, for particles stopped in PD1, and a more curved part for particles punching through the PD1 photodiode and stopped in the CsI1 crystal. Due to line crossing and its complex structure, this kind of a map cannot be used for identification, however thanks to the presence of many characteristic punch-through points and curvatures, it is very well suited for energy calibration purposes.

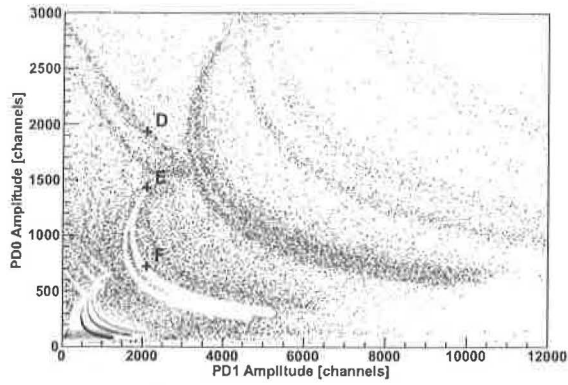


Figure 6: ΔE -E ID map for PD0 vs PD1(SCT), for particles stopped in PD1 or in CsI1.

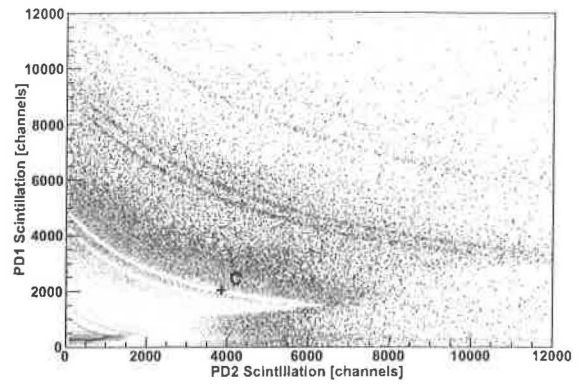


Figure 7: ΔE -E ID map of scintillation signals for CsI1 vs CsI2 detected by PD1 and PD2.

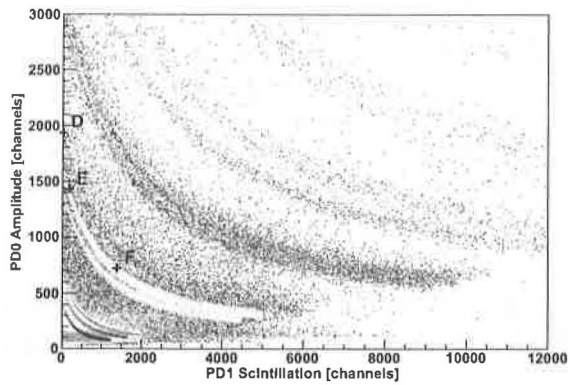


Figure 8: Decomposition of the map from Fig. 6. PD0 vs scintillation detected by PD1 - for particles stopped in CsI1.

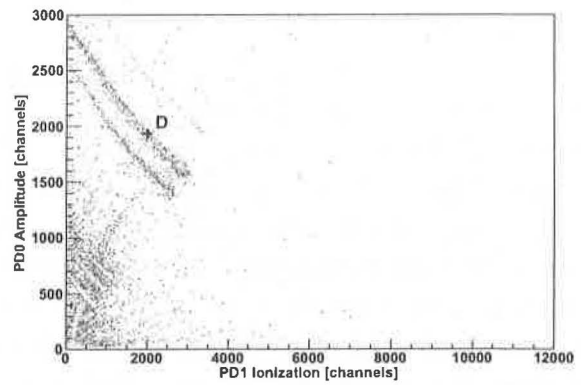


Figure 9: Decomposition of the map from Fig. 6. PD0 vs ionization signal from PD1 - for particles stopped in PD1 (producing no light).

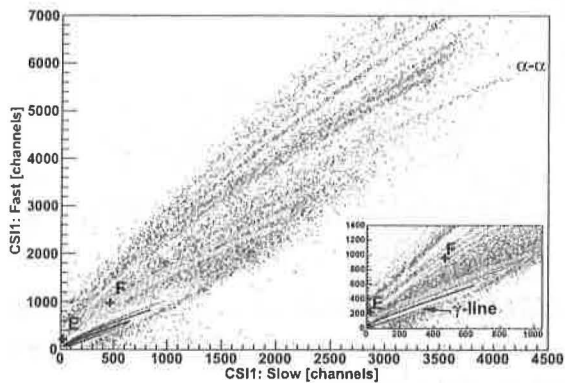


Figure 10: Fast vs Slow components of the scintillation in CsI1. The inset shows more clearly a γ -line and the p , d , t lines.

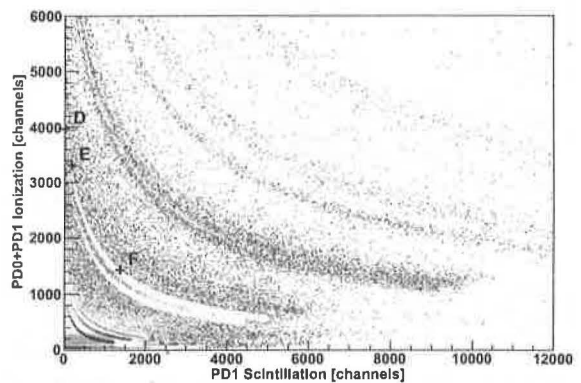


Figure 11: Summed PD0+PD1 ionization components vs scintillation in PD1 for particles stopped in CsI1.

Fig. 7 shows a ΔE -E map for scintillation signals detected by a second vs third photodiode. Apart from the very good isotopic resolution, one can see a substantial background from the secondary reactions/scatterings in the crystals and also from particles crossing the module at an angle and not originating from the target, as well as back-bendings corresponding to particles punching through the thick crystal (see discussion at the end of this section).

Thanks to the pulse shape decomposition, the ionization component for particles hitting the photodiode (*nuclear counter effect*) at the back of the thick crystal has been easily removed.

Using the individual reconstructed amplitudes for the ionization and for the scintillation components, the map of Fig. 6 can be decomposed into the PD0-PD1(Si) and PD0-PD1(CsI) components of the SCT segment (Figs. 9 and 8). This makes effectively KRATTA even a four-fold telescope.

The isotopic resolution visible from Fig. 8 can be improved by summing up the reconstructed ionization components from PD0 and PD1, and thus, increasing the effective thickness of the first ΔE layer to 1 mm of Si. See also inset in Fig. 14. Fig. 11 presents a classical ΔE -E ID map obtained from Fig. 6 thanks to the pulse shape decomposition (see discussion of Fig. 17 for more details on this transformation and Fig. 14 for the corresponding mass resolution.)

Figures 10 and 12 show the “Fast-Slow” ID maps for the CsI1 and CsI2 crystals, respectively. The latter represents a variant of the standard representation, using the total light vs the ratio Slow over Fast (see e.g. [18]). The Fast-Slow representation is very useful in many respects in addition to the standard ΔE -E one: One can observe a clear double alpha line (α - α in Figs. 10 and 12) which is hidden in the ΔE -E representation behind the Li isotope lines. The Fast-Slow map shows a clear “ γ -line” - a strong line below the proton line due to γ -rays (see inset in Fig. 10), which can be precisely isolated and removed from the ΔE -E map. Last, but not least, as can be seen from Fig. 12, the punch through segments do not cross the lower lying isotope lines in a way they do in case of the ΔE -E maps (Fig. 7). Thus, the Fast-Slow maps allow to isolate the punch through segments in a much more precise way. Unfortunately, the punch through segments eventually merge with the γ -lines, which makes it difficult to discriminate between these two.

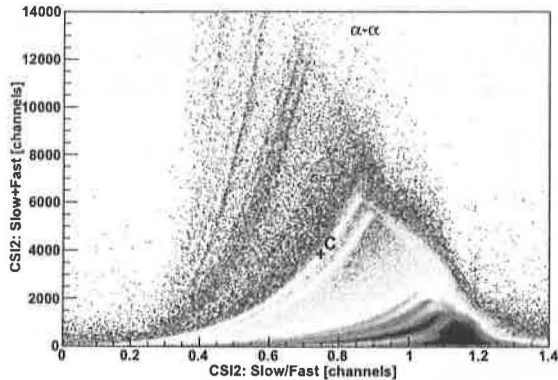


Figure 12: Total light vs Slow over Fast components of the scintillation in CsI2. Note, that unlike in Fig. 7, the punch through lines do not cross the lower lying isotope lines.

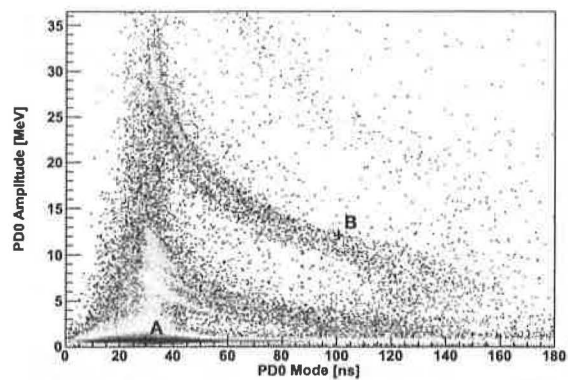


Figure 13: Amplitude vs mode of the current signal for particles stopped in PD0, obtained from a single Si chip.

Figure 13 demonstrates yet another powerful feature of the pulse shape analysis. It allowed to perform an identification of the majority of light particles stopped in the first photodiode by plotting the amplitude vs mode of the reconstructed current signal (6). Due to the constant value of the field within the intrinsic region of the PIN diode the enhancement of the resolution for stopped particles is not expected to be as pronounced as in the case of reverse mount PN detectors [19], nevertheless, the relation between the range and the carrier collection time seems to be still strong enough to enable the isotopic separation of light particles. This method allowed to reduce the lower identification threshold, due to the thickness of the

first photodiode, (see Table 2) from 8.3 to about 2.5 MeV for protons, where they are still resolvable from deuterons (see two bottom lines in Fig. 13). This effectively corresponds to the reduction of the thickness of the first ΔE layer from 500 to about 65 μm of Si.

One should stress, that the time scale presented in Fig. 13 exceeds by about a factor of 3 the collection times estimated on the basis of the mobilities of the carriers alone, thus the plasma delay, or other effects, seem to be quite important in slowing down the collection process.

The mass resolution for particles stopped in the thin crystal (CsI1) and in the thick one (CsI2) can be viewed from Figs. 14 and 15, respectively.

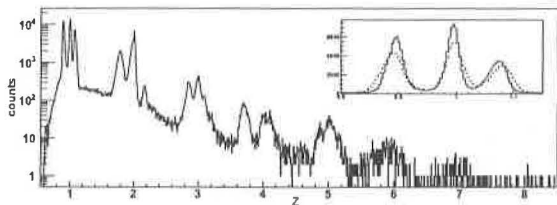


Figure 14: Particle identification spectrum (charge distribution) obtained from the map of Fig. 11, for particles stopped in CsI1.

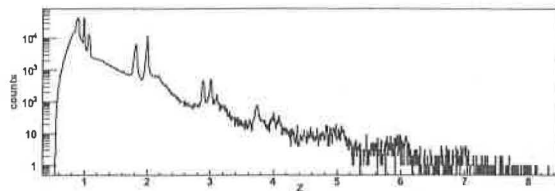


Figure 15: Same as Fig. 14, but obtained from the map of Fig. 7, for particles stopped in the thick crystal.

The background in Fig. 14, resulting mainly from the secondary reactions/scattering in the crystal, amounts to about 6% for the hits below the p , d , t peaks. For energetic $Z = 1$ particles traversing the thick crystal (12.5 cm of CsI) the secondary reaction probability amounts to about 46% (Fig. 15). These probabilities agree reasonably well with the simple estimates obtained using the nuclear collision length of 22.30 cm for CsI [20], which yields the probabilities of 11% and 43% for 2.5 and 12.5 cm of CsI, respectively. The background measured under the p , d , t lines includes also some contribution from the secondary reactions of neutrons and heavier charged particles, as well as from the accidental coincidences. The γ and punch-through hits have been removed from the background, in both cases. The high secondary interaction probability obviously deteriorates the identification quality and defines the limits for applying the telescope method to intermediate energies.

6. Discussion and remarks

Since the parametrization of the pulse shapes is only approximate and has no deep physical background, one can ask how precise is the decomposition into individual components and how physical they are. In order to address these questions, the ΔE -E map of the SCT (PD1+CsI1) has been compared to the predictions of the ATIMA range-energy tables. Such a comparison requires the knowledge of the energy calibration of both, the silicon photodiodes and of the CsI(Tl) light output. The calibration has been performed using the ID map of Fig. 6 (see Fig. 16) which is relatively insensitive to the details of the decomposition and is perfectly suited for the energy calibration due to its richness in characteristic punch-through points and curvatures.

The calibration routine allowed to adjust the thicknesses of the dead and active layers, the energy calibration parameters, as well as the light-energy conversion parameters. For the latter, a simple integrated Birks' formula (see e.g. [16]) has been used, with $dE/dx \propto AZ^2/E$, yielding a commonly applied two-parameter Light-Energy relation [21], applicable

for particles stopped in the scintillator:

$$\text{Light} = a_1 \left(E - a_2 A Z^2 \log \left[1 + \frac{E}{a_2 A Z^2} \right] \right) \quad (7)$$

with E being the energy, A, Z - mass and atomic numbers of the stopped particle, a_1, a_2 - the gain and quenching parameters.

Having this (inverse) calibration it was possible to superpose the ATIMA lines on the decomposed ID map for the Single Chip Telescope segment of the KRATTA module. The result is presented in Fig. 17 and is worth a comment.

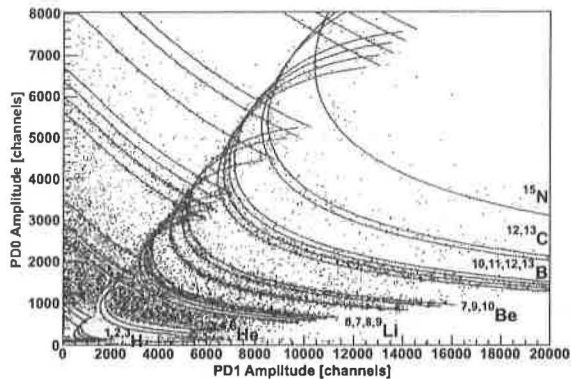


Figure 16: Same as Fig. 6 but with the superimposed ID lines calculated using the ATIMA range-energy tables.

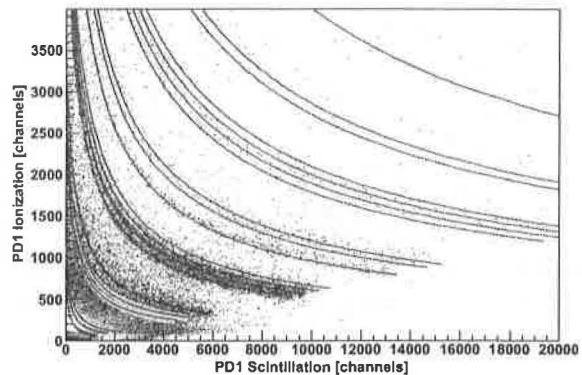


Figure 17: Decomposed SCT ΔE -E identification map with the superimposed ATIMA lines. The sequence of lines is the same as in Fig. 16.

The observed very good agreement between the reconstructed amplitudes and the range-energy table predictions is quite non-trivial taking into account the simplicity of the pulse shape parametrization. In order to obtain this kind of agreement, which is still a compromise, it was not enough to set all the parameters free and search for the minimum of the χ^2 distribution. Such an automatic procedure guarantees the best fit to the waveforms, but not necessarily guarantees the follow up of the trends defined by the range-energy tables. In general, an automatic procedure can lead, depending also on the starting values, to some local minima, produce discontinuities or lead in directions diverging from the ATIMA lines. The presented agreement has been obtained after searching for the optimal values and fixing some of the parameters (see Table 3). The agreement with the ATIMA lines could be made even better, for instance by freeing the τ_{RS} parameter, however at the expense of losing completely the mass resolution in Fast-Slow representation (contrary to the case presented in Fig. 10). Thus, the presented agreement is a result of an iterative procedure of fixing some of the parameters and also of the energy calibration parameters, but once the crucial parameters are constrained the fitting proceeds automatically.

The whole procedure could probably be better automatized by using more realistic pulse shape parametrizations, especially for individual electron and hole components of the ionization signal, taking into account the plasma delay effects, interactions between carriers, diffusion effects, etc [15]. However, to our knowledge, such pulse shape parametrizations are still to be developed. Definitely, a more realistic preamplifier response function would improve the resolution and would allow for disentangling between physical and instrumental parameters. A more realistic parametrization and analysis would be worth the effort of implementing it to e.g. better understand the relation between the range and the charge collection times which enable the identification of the particles stopped in the silicon detectors.

Nevertheless, any more sophisticated analysis would definitely slow down even more the analysis.

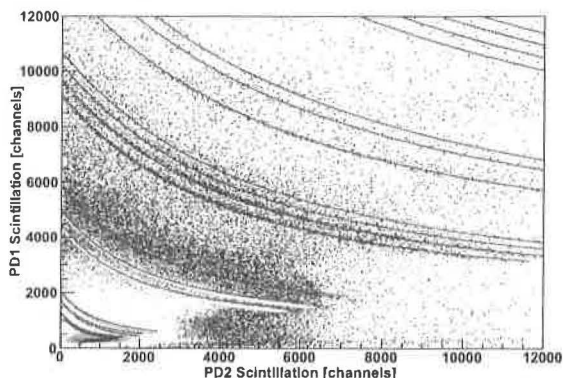


Figure 18: ΔE -E identification map for scintillation signals from CsI1 vs CsI2, with the superimposed ID lines calculated using the ATIMA tables. The sequence of lines is the same as in Fig. 16. The γ -line and punch-through hits have been removed (cf. Fig. 7).

Finally, Fig. 18 shows the calculated ATIMA lines superimposed on the ΔE -E identification map for scintillation signals from thin vs thick CsI(Tl) crystals. The slight overestimation of the ΔE component for $Z = 1$ particles results most probably from the simplicity of the Light-Energy conversion formula (7) and (or) from the light output non-uniformity of the crystals. The overall agreement is, nevertheless, quite satisfactory and the calculated lines can be used not only to derive the energy calibration parameters, but also for identification (see Fig. 15), after small manual adjustments.

The energy calibration routine based on the ATIMA range-energy tables operated on all three maps (Figs. 16-18) simultaneously, allowing for a consistent determination of the calibration parameters for all photodiodes and both crystals. Specifically, for the CsI(Tl) crystals with 1500 ppm of Tl concentration, the quenching parameter a_2 was found to be equal to 0.32, a value compatible with the one from [21] and about 20% larger than the average one quoted for the INDRA crystals [22]. The calibration of the SCT allowed also to estimate the efficiency of the scintillation. The combination of a relatively high Tl doping, high reflectance of the wrapping and large active area of the photodiode, resulted in a relatively high efficiency for energy-light conversion. It was found that only about 6 times more energy was needed to produce an electron-hole pair in the photodiode through a scintillation process in the CsI(Tl) crystal than in the direct ionization process in the photodiode. This fact is worth noting, since for the “good scintillators” quoted in [16] this factor amounts to 15-20.

Obviously, a drawback of the telescope method at high energies, is the high level of the secondary reactions. In order to handle this problem, a more sophisticated methods, neural networks and discriminant analysis are being tested, but this goes beyond the scope of this contribution.

Summary

A new, low threshold, broad energy range, versatile array of triple telescopes, KRATTA, has been constructed. The modules, equipped with digital electronics chains, allowed for isotopic identification of light charged reaction products.

Pulse shape analysis allowed for realistic decomposition of the complex SCT pulse shapes into individual ionization and scintillation components and eventually profit from the, otherwise harmful, nuclear counter effect. The isotopic resolution obtained using a single readout channel was found to compete very well with those obtained using the standard

two channel readout. The applied pulse shape analysis permitted also the identification of particles stopped in the first photodiode and the reduction of the identification threshold, due to the thickness of the first photodiode, by a factor of three. Thanks to the pulse shape analysis, it was also possible to obtain the ballistic deficit free amplitudes, which allowed for easy energy calibration and identification based on the predictions of the range-energy tables.

The array has met the expectations, fulfilled the design requirements and performed very well during the ASY-EOS experiment at GSI.

Acknowledgments

Work made possible through funding by Polish Ministry of Science and Higher Education under grant No. DPN/N108/GSI/2009.

We (S.K.) acknowledge the support by the Foundation for Polish Science - MPD program, co-financed by the European Union within the European Regional Development Fund.

Stimulating discussions, expertise and help of Giacomo Poggi as well as of Marian Pârlog, Remi Bougault and Hector Alvarez Pol during the design and test phase of the prototypes are gratefully acknowledged.

References

- [1] P. Russotto et al., IWM 2011 Proc., Conf. Proc. Vol. 105, p. 91. P. Russotto et al., IWM 2009 Proc., Conf. Proc. Vol. 101, p. 22. <http://www.irb.hr/users/mkis>. <http://www.ct.infn.it/asyeos2010>. P. Russotto et al., Phys. Lett. B 697 (2011) 471.
- [2] Th. Blaich et al., Nucl. Instr. Meth. A 314 (1992) 136. P. Pawłowski et al., Nucl. Instr. Meth. A 694 (2012) 47.
- [3] A. Pagano et al., Nucl. Phys. A 734 (2004) 504.
- [4] A. Schüttauf et al., Nucl. Phys. A 607 (1996) 457.
- [5] HAMAMATSU Si Photodiode for Direct Detection (S5377-0052(X)).
- [6] Manufacturer: Institute of Modern Physics, Chinese Academy of Sciences, Lanzhou, China.
- [7] G. Pasquali et al., Nucl. Instr. Meth. A 301(1991) 101.
- [8] 3M VikuitiTM ESR foil, recommended by the crystal manufacturer.
- [9] <http://www-linux.gsi.de/~weick/atima>
- [10] Z. Sosin et al., in preparation.
- [11] CAEN V1724 digitizer.
- [12] http://www.gsi.de/informationen/wti/ee/elekt_entwicklung/triva_e.html
- [13] RIO4-8072RE, CES, <http://www.ces.ch>
- [14] <http://www-win.gsi.de/daq/>
- [15] C.A.J. Ammerlaan et al., Nucl. Instr. Meth. 22 (1963) 189. A. Alberigi Quaranta et al., Nucl. Instr. Meth. 57 (1967) 131. G. Pausch et al., Nucl. Instr. and Meth. A 337 (1994) 573. M. Pârlog et al., Nucl. Instr. Meth. A 613 (2010) 290. Z. Sosin, Nucl. Instr. Meth. A 693 (2012) 170.
- [16] G.F. Knoll, "Radiation Detection and Measurement", 4-th ed., Wiley (2010), Chapt. 9, 16.
- [17] <http://root.cern.ch>. A.J. Ketikian et al., Nucl. Instr. and Meth. A 314 (1992) 578. S.N. Dymov et al., Nucl. Instr. and Meth. A 440 (2000) 431.
- [18] F. Benrachi et al., Nucl. Instr. and Meth. A 281 (1989) 137.
- [19] G. Pausch et al., Nucl. Instr. and Meth. A 365 (1995) 176. L. Bardelli et al., Nucl. Instr. and Meth. A 654 (2011) 272.
- [20] http://pdg.lbl.gov/2012/AtomicNuclearProperties/HTML_PAGES/141.html
- [21] D. Horn et al., Nucl. Instr. and Meth. A 320 (1992) 273.
- [22] M. Pârlog et al., Nucl. Instr. and Meth. A 482 (2002) 693.